

AN IMPROVED METHOD OF BUSBAR VOLTAGE RECONSTRUCTION FROM SIGNALS OF ELECTRIC FIELD SENSORS INSTALLED IN AN INDOOR MV SUBSTATION

Dariusz Borkowski

AGH – University of Science and Technology, Faculty of Electrical Engineering, Automatics, Computer Science and Biomedical Engineering, Al. A. Mickiewicza 30, 30-059 Cracow, Poland (✉ borkows@agh.edu.pl, +48 12 617 2841)

Abstract

This paper presents an improved method for the reconstruction of busbar voltage waveforms from signals acquired by a system of electric field (EF) sensors located in an indoor medium voltage substation. In the previous work [8], the authors proposed the use of black-box models in the form of artificial neural networks (ANNs) for this task. In this paper it is shown that a parametric model of the system of EF sensors can reconstruct voltages with much lower errors, provided that it is accurately identified. The model identification is done by minimization of a nonlinear goal function, i.e. mean squared error (MSE) of voltage reconstruction. As a result of examining several optimization techniques, the method based on simulated annealing extended with a simplex search, is proposed. The performance of the model identified with this method is at least 8 times better in terms of MSE and at least 12 times better in terms of frequency domain errors than the best one of concurrent ANNs.

Keywords: voltage measurement, signal reconstruction, modelling, parameters identification, simulated annealing.

© 2018 Polish Academy of Sciences. All rights reserved

1. Introduction

Precise measurement of instantaneous voltage is essential for power grid control and for the settlements of energy. It is also needed for the calculation of active and reactive power, harmonic impedance measurement [1], etc.

Inductive voltage transformers (IVTs) are commonly used in medium voltage (MV) grids and high voltage (HV) grids due to their acceptable cost and galvanic insulation between primary and secondary circuits. However, with the increase of primary voltage their frequency band is limited [2]. Another group of measurement transducers are those based on capacitive electric field (EF) sensors or multiple EF sensors. These transducers provide galvanic insulation at a low cost and limited space requirements. The problems arise because of the presence of stray fields and unknown or sometimes also a varying geometry of the system of sensors and observed voltage lines [3]. The EF-based methods differ in respect of the measurement goal, observed voltage level, fixed/varying or known/unknown geometry. Some transducers and methods are

dedicated only to voltage detection [4], some other enable the calculation of aggregated voltage parameters, like e.g. THD factor [5] or RMS voltage [4].

There are very few reported EF-based methods which are able to reconstruct voltage waveforms in a wide band. The method presented in [6] is aimed for low voltage monitoring in a smart meter by means of miniature cylindrical EF transducers installed around phase wires, while the method proposed in [7] is used to monitor HV overhead lines with 3 planar EF sensors, one per phase. In [6] unknown capacitances are estimated by switching two configurations of the input filter. In [7] unknown capacitances are estimated either from line tripping transients or by calculations made with the assumption of symmetrically installed sensors. The method in [8] can reconstruct indoor MV substation busbar voltages from a fixed geometry system of 5 EF sensors located under busbars, using an artificial neural network (ANN) which is trained beforehand with reference sensors. In each of these methods the main problem is the selection of the model and its identification.

Such an indirect voltage measurement can be decomposed into two stages: conversion and reconstruction ones [9]. The conversion stage includes the transformation of busbar voltages \mathbf{u}_B into the digital form of EF sensor voltages \mathbf{u}_S , while in the reconstruction stage an inverse mathematical model is applied with its outputs being estimates $\hat{\mathbf{u}}_B$ of busbar voltages \mathbf{u}_B (Fig. 1).

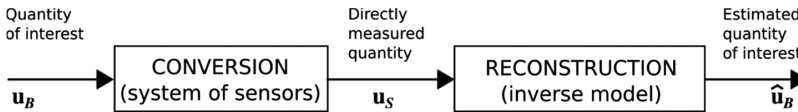


Fig. 1. Measurement of busbar voltages decomposed into two stages.

In the case of substation busbar voltage measurement the distances between sensors and busbars are high enough to provide each sensor with the possibility of simultaneous measurement of EFs coming from all busbars. This coupling has to be taken into account in modelling. It also makes an inverse model, used for busbar voltages reconstruction, a nonlinear function of multiple parameters.

Nonlinear dynamic models can be black-box ones, like ANNs, or parametric ones with a structure reflecting the structure of the object selected features of the object (dynamics, non-linearity, etc.) [10]. The application of a black-box model in the form of an ANN requires the selection of ANN structure (number of neurons, activation functions, etc.) and its training, usually done by dedicated optimization methods [8]. The application of a parametric model requires the selection of the model structure and order, and then determination of its parameter values. Numerous model structures can be used: Volterra series [11], Viener–Hammerstein models [10], multi-model (combination of several local models) [12], nonlinear dynamic models (NARX, etc.) or equivalent circuits. Also, numerous identification methods can be used in the second stage, including common optimization techniques [13].

In the previous work [8], black-box models in the form of ANNs trained in the supervised mode, using EF sensor voltages as inputs and known busbar voltages as targets, were employed for the reconstruction of 3-phase busbar voltages. In the same paper an equivalent circuit model, composed of actual object capacitances and susceptances, was proposed as the reference method. Parameter values of the equivalent circuit were determined by the direct measurement with an Agilent E4980A LRC meter. Despite using the precise meter, errors of model parameters' determination were high enough to consider the reference method as a poor one with respect to the considered ANNs.

In this paper an improved method for the reconstruction of busbar voltages by the parametric model is proposed and validated. The model is the inversed conversion stage, based on the structure of the system of busbars and EF sensors. Accurate identification of this model is not a trivial task, as the goal function (MSE of busbar voltage reconstruction) is nonlinear and a number of suboptimal solutions hinders its identification, what causes that several classic optimization methods fail. Therefore, the choice of an optimization method is critical. It is shown that busbar voltages can be reconstructed by an accurately identified inverse model with significantly lower errors than those obtained with the ANNs from [8] exhibiting the best performance.

The structure of the paper is as follows. Section 2 describes the object of identification and the derivation of the model. In Section 3 the general idea of model identification by minimization of voltage reconstruction errors as well as the analysis leading to the selection of a minimization method are given. In Section 4 the results of model verification in the time and frequency domains are shown and compared with the best ANN from [8]. Section 5 concludes the paper.

2. Model design

The object of interest was an indoor 15 kV substation, supplied from a 0.4/15 kV step-up transformer. The substation was equipped with 3 reference resistive voltage dividers (RVDs) of declared 1% AC accuracy from 10 Hz to 1.6 MHz for recording object outputs (Fig. 2).

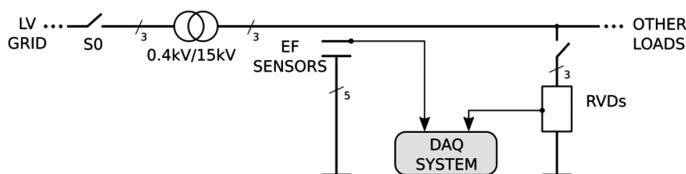


Fig. 2. A schematic of substation.

Five EF sensors, build of small metal plates 6×8 cm each, were installed in the overhead compartment of the substation, centrally below busbars, 2 cm above the grounded common plate placed on the floor of the compartment (Fig. 3).

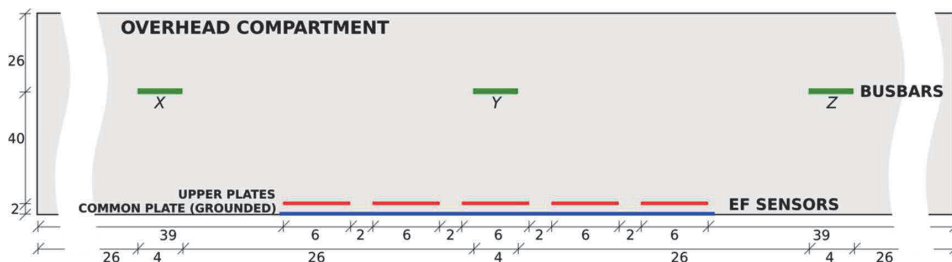


Fig. 3. A placement of sensors (dimensions in cm, proportions not maintained).

A small, 2 cm, displacement between adjacent sensors did not assure sufficient separation of signals, however five sensors (instead of three) gives redundant information, which enables to limit the impact of measurement noise. The system composed of capacitances between sensors, busbars, the ground plate as well as shielded cables and input impedances was actually the object of identification. A single measurement channel is shown in Fig. 4.



Fig. 4. A single measurement channel with EF sensor.

2.1. Physical model derivation

The object geometry is the basis for the creation of its equivalent circuit (Fig. 5), which includes most significant capacitances, i.e.: busbars-to-sensors capacitances C_{Xi} , C_{Yi} , C_{Zi} , $i = 1, \dots, 5$, sensors-to-ground capacitances C and capacitances between adjacent sensors C_A . The cable and ADC parameters are included in sensor capacitance C and parallel susceptance B .

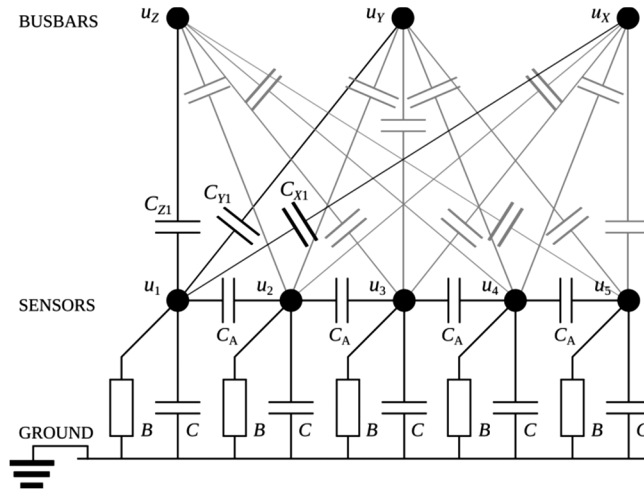


Fig. 5. The equivalent circuit of a system of EF sensors. Capacitances between busbars and sensors 2 to 4 (grey) are left without descriptions for the clarity. All capacitances (both black and grey ones) are included in the model.

From the circuit structure, the following linear equations (1) were derived using the Kirchoff's current law for each sensor node:

$$\begin{aligned}
 C_{X1}\dot{u}_X + C_{Y1}\dot{u}_Y + C_{Z1}\dot{u}_Z &= C\dot{u}_1(t) + C_A(\dot{u}_1 - \dot{u}_2) + Bu_1, \\
 C_{X2}\dot{u}_X + C_{Y2}\dot{u}_Y + C_{Z2}\dot{u}_Z &= C\dot{u}_2(t) + C_A(\dot{u}_2 - \dot{u}_1) + C_A(\dot{u}_2 - \dot{u}_3) + Bu_2, \\
 C_{X3}\dot{u}_X + C_{Y3}\dot{u}_Y + C_{Z3}\dot{u}_Z &= C\dot{u}_3(t) + C_A(\dot{u}_3 - \dot{u}_2) + C_A(\dot{u}_3 - \dot{u}_4) + Bu_3, \\
 C_{X4}\dot{u}_X + C_{Y4}\dot{u}_Y + C_{Z4}\dot{u}_Z &= C\dot{u}_4(t) + C_A(\dot{u}_4 - \dot{u}_3) + C_A(\dot{u}_4 - \dot{u}_2) + Bu_4, \\
 C_{X5}\dot{u}_X + C_{Y5}\dot{u}_Y + C_{Z5}\dot{u}_Z &= C\dot{u}_5(t) + C_A(\dot{u}_5 - \dot{u}_4) + Bu_5,
 \end{aligned} \tag{1}$$

where X, Y, Z are phase indexes, u_X, u_Y, u_Z are busbar voltages, u_1, \dots, u_5 are sensor voltages and "dot" symbol denotes the first derivative over time.

After the integration of (1) over time it can be rewritten in the matrix form:

$$\mathbf{C}_B \mathbf{u}_B(t) = \mathbf{C}_S \mathbf{u}_S(t) + B \int_0^t \mathbf{u}_S(\tau) d\tau, \quad (2)$$

where

$$\mathbf{u}_B(t) = [u_X(t) \ u_Y(t) \ u_Z(t)]^T, \quad \mathbf{u}_S(t) = [u_1(t) \ u_2(t) \ u_3(t) \ u_4(t) \ u_5(t)]^T,$$

$$\mathbf{C}_B = \begin{bmatrix} C_{X1} & C_{Y1} & C_{Z1} \\ C_{X2} & C_{Y2} & C_{Z2} \\ C_{X3} & C_{Y3} & C_{Z3} \\ C_{X4} & C_{Y4} & C_{Z4} \\ C_{X5} & C_{Y5} & C_{Z5} \end{bmatrix}, \quad \mathbf{C}_S = \mathbf{C}\mathbf{I} + \begin{bmatrix} C_A & -C_A & 0 & 0 & 0 \\ -C_A & 2C_A & -C_A & 0 & 0 \\ 0 & -C_A & 2C_A & -C_A & 0 \\ 0 & 0 & -C_A & 2C_A & -C_A \\ 0 & 0 & 0 & C_A & C_A \end{bmatrix},$$

and \mathbf{I} is an identity matrix.

By solving (2) in the least square sense an inverse model of the EF sensors' system, which expresses estimates of busbar voltages as a function of EF sensor voltages, was obtained:

$$\hat{\mathbf{u}}_B(t) = \underbrace{(\mathbf{C}_B^T \mathbf{C}_B)^{-1} \mathbf{C}_B^T}_{\mathbf{K}_B} \left(\mathbf{C}_S \mathbf{u}_S(t) + B \int_0^t \mathbf{u}_S(\tau) d\tau \right). \quad (3)$$

After the discretization, the model (3) can be used for the reconstruction of busbar voltages. The signal processing path of busbar voltage reconstruction is shown in Fig. 6.

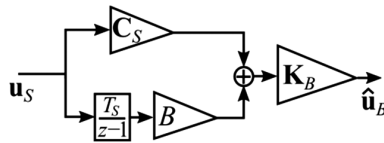


Fig. 6. A block diagram of signal reconstruction in the matrix-vector form.

The pseudoinverse \mathbf{K}_B of matrix \mathbf{C}_B can be pre-calculated. Then the calculation of busbar voltages' vector uses only 65 floating point math operations (additions and multiplications) per sampling period. It can be performed even by a low-cost CPU. The group delay introduced by the model is only half of sample, thus the model can be successfully used in protective automation, as it presents a real-time behaviour.

3. Model identification

3.1. Acquisition of identification and verification datasets

The ground-referenced EF sensor voltages were recorded using an NI CompactRIO system equipped with 24-bit ADCs of ± 10.52 V range. The RVD voltages were recorded synchronously with EF sensor voltages using the same data acquisition system but equipped with 24-bit 300 V_{RMS} ADCs. 10 kHz sampling rate was used. After the identification the RVDs are no

longer needed and can be removed. The procedures of identification and verification of the model were performed offline, after disassembling the setup and removing the substation equipment.

During the experiment steady-state voltages interleaved with voltage sags, generated by manual tripping of S0 switch (Fig. 2), were recorded. Different patterns of voltage unbalance during transients were obtained due to the random non-simultaneity of the opening of phase contacts of the switch.

From the entire record two 8000-sample long (0.8 s) datasets were extracted for the purpose of model identification: the SS dataset containing steady-state voltages only and the SD dataset containing a voltage sag. Additionally, two 120 s long datasets were extracted for the purpose of model verification: the SS dataset containing steady-state voltages only and the SD dataset containing steady-state voltages interrupted by 3 sags.

Each dataset was composed of recorded sensor voltages (inputs) and busbar voltages (outputs). Busbar voltages from the identification and verification datasets are shown in Fig. 7 and Fig. 8, respectively.

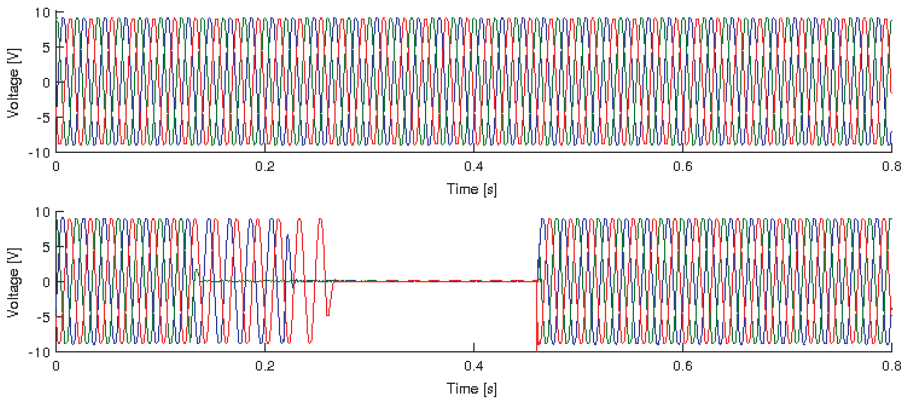


Fig. 7. The object output (RVD voltages) used for model identification. SS dataset (top), SD dataset (bottom).

It should be mentioned that even SS datasets contain small disturbances, not visible in the scale of Fig. 8, resulting from supplying the object directly from the real power grid.

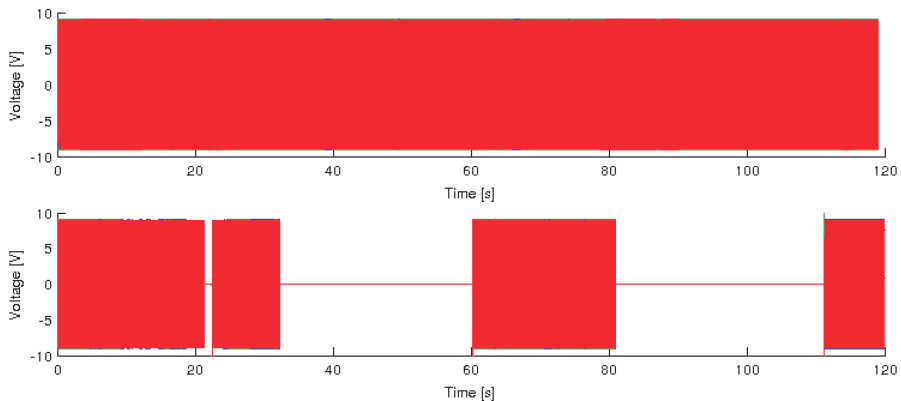


Fig. 8. The object output (RVD voltages) used for model verification. SS dataset (top), SD dataset (bottom).

In order to verify methods in noisy conditions additional verification datasets SSN and SDN were created by adding white Gaussian noise (40 dB SNR) to input signals in SS and SD verification datasets, respectively.

3.2. Model identification scheme

The model parameters were identified by minimization of mean squared error (MSE) of busbar voltages' reconstruction over all phases:

$$MSE(\mathbf{x}) = \frac{1}{3} \sum_{p \in X, Y, Z} \left(\frac{1}{N} \sum_{n=1}^N (\hat{\mathbf{u}}_B(p, n, \mathbf{x}) - \mathbf{u}_B(p, n))^2 \right). \quad (4)$$

where n is a time index, p is a phase (busbar) index, \mathbf{x} is a vector of model parameters, $\mathbf{u}_B(p, n)$ is an actual p -th busbar voltage waveform (object output) measured by p -th RVD, while $\hat{\mathbf{u}}_B(p, n, \mathbf{x})$ is a reconstructed p -th busbar voltage waveform (model output).

For each examined identification method, the starting point \mathbf{x}_0 for the minimization was a vector composed of directly measured capacitances and susceptance in the following order: $[C_{X1}, \dots, C_{X5}, C_{Y1}, \dots, C_{Y5}, C_{Z1}, \dots, C_{Z5}, C_A, C, B]^T$.

In each iteration of the minimization loop, the model outputs $\hat{\mathbf{u}}_B$ were calculated by filtering the model inputs \mathbf{u}_S through the discretized model (3) using the current set \mathbf{x} of model parameters. Then the MSE was calculated and the model parameters were updated accordingly.

3.3. Selection of minimization method

Finding the minimum of the goal function (4) requires the application of a nonlinear optimization method, because the model (3) is a nonlinear function of its parameters. The number of parameters of the model makes it difficult to assess the number of minima the goal function can have. Due to the pseudo-inversion of \mathbf{C}_B matrix discontinuities and/or singularities can be present in the goal function. Thus the selection of a minimization method was not trivial, as some methods failed and some others led to a feasible but not sufficiently good solution.

Initially, local nonlinear optimization methods were examined in order to check whether they are able to find a suboptimal but sufficient solution, i.e. a set \mathbf{x} of model parameters, for which the reconstruction errors are lower than for the best ANNs from [8]. The selected methods were: unconstrained BFGS method [14], constrained interior point method [15] and unconstrained simplex method [16].

The BFGS method failed in the starting point, because it could not decrease the value of objective function by moving along the calculated search direction. The interior point method always failed at bounds of the search region defined as $[0.1 \cdot \mathbf{x}_0, 10 \cdot \mathbf{x}_0]$. Extending the search region did not help.

The simplex method converged to a feasible local solution and gave twice lower MSE than the best ANN (LYRC-5-L) from [8]. It shifted model parameters by at most 20% from the starting point. However, in the frequency domain, it gave the maximum error (7) of magnitude greater by 36 % than LYRC-5-S (the second best ANN from [8]).

Then, the unconstrained global minimization simulated annealing (SA) technique was examined. The SA, in its pure form [17], converged to a feasible solution, but the performance of the identified model was not satisfactory [18] (MSE of voltage reconstruction was about 22 times higher than that obtained with LYRC-5-L). Thus, the global SA minimization was extended by an additional local search (a so-called hybrid method) repeated every given number of iterations.

Such an approach complements the random characteristic of SA by the precise location of local minima [19]. The simplex method was selected as a hybrid method in the global minimization routine, due to its proper behaviour in the local minimization task. The hybrid method was executed every 50 iterations of global minimization loop and yet once more after satisfying the termination criteria.

Such a combined minimization method, called SASC (simulated annealing + simplex combined), converged to the best among all solutions in terms of both MSE and frequency domain errors of voltage reconstruction. Thus, the SASC method was selected for model identification. In all tested cases this technique led to a feasible solution, keeping the parameter values within physically acceptable bounds. The results obtained with considered minimization methods are summarized in Table 1 (TD means time domain, FD – frequency domain and E_M – magnitude error (7) in FD).

Table 1. Verification results obtained with considered methods.

Domain / Dataset	TD / SD	FD / SS	FD / SS	
Method / error	MSE	$\max(E_M)$	$\text{mean}(E_M)$	Result comment
BFGS	1.421	8.63	0.1	stuck at starting point
Interior point	0.344	4.32	0.052	ends always on boundary
Simplex	0.0103	1.69	0.0244	feasible
Simulated Annealing	0.431	9.27	0.0461	feasible
SASC-SD	0.0023	0.35	0.0073	feasible (best of all)
LYRC-5-L	0.0202	7.07	0.0919	feasible (best ANN)
LYRC-5-S	0.141	1.24	0.0311	feasible (second best ANN)

3.4. Identification method

The proposed identification method is limited to the identification of EF sensors system installed in an overhead compartment of an indoor substation. Such a constraint limits variations of some environmental factors like temperature and humidity, which are not included in the model. The location of sensors inside the overhead compartment also limits the impact of external electric fields, as EF sensors are shielded by the grounded substation housing.

Generally, the identification steps are as follows:

- 1) install the system of EF sensors and reference transducers (e.g. RVDs); prepare data acquisition system, which is able to simultaneously sample recorded voltages;
- 2) design a circuit model based on the number of sensors and main capacitances present in the system; derive the inverse model for voltage reconstruction;
- 3) measure main capacitances in the system in order to determine the starting point \mathbf{x}_0 for the identification;
- 4) record steady-state busbar voltages interrupted by some transients and imbalance regions; record inputs (EF sensor voltages) and outputs (RVD voltages);
- 5) prepare identification and verification datasets from the recorded signals;
- 6) identify the model with the identification dataset and the proposed SASC technique; check the feasibility of the solution;

- 7) verify the performance of the model with the verification dataset;
- 8) if the performance is not acceptable, repeat the process (try to modify optimization parameters, the starting point, revise the model or prepare better datasets);

A diagram of the SASC minimization algorithm is shown in Fig. 9. The meaning of variables is as follows: \mathbf{x}_{curr} is a solution in current i -th iteration; F_{curr} is an MSE value at \mathbf{x}_{curr} ; a is a counter of accepted solutions; T is a scale used for randomization of \mathbf{x}_{curr} and conditional random acceptance of worse solutions; I_H is the number of iterations, after which the hybrid method is run; I_R is the number of accepted solutions, after which reannealing is performed; k is a parameter used for T update. \mathbf{x}_{best} and F_{best} are the best up-to-date solution and MSE value in this solution, respectively.

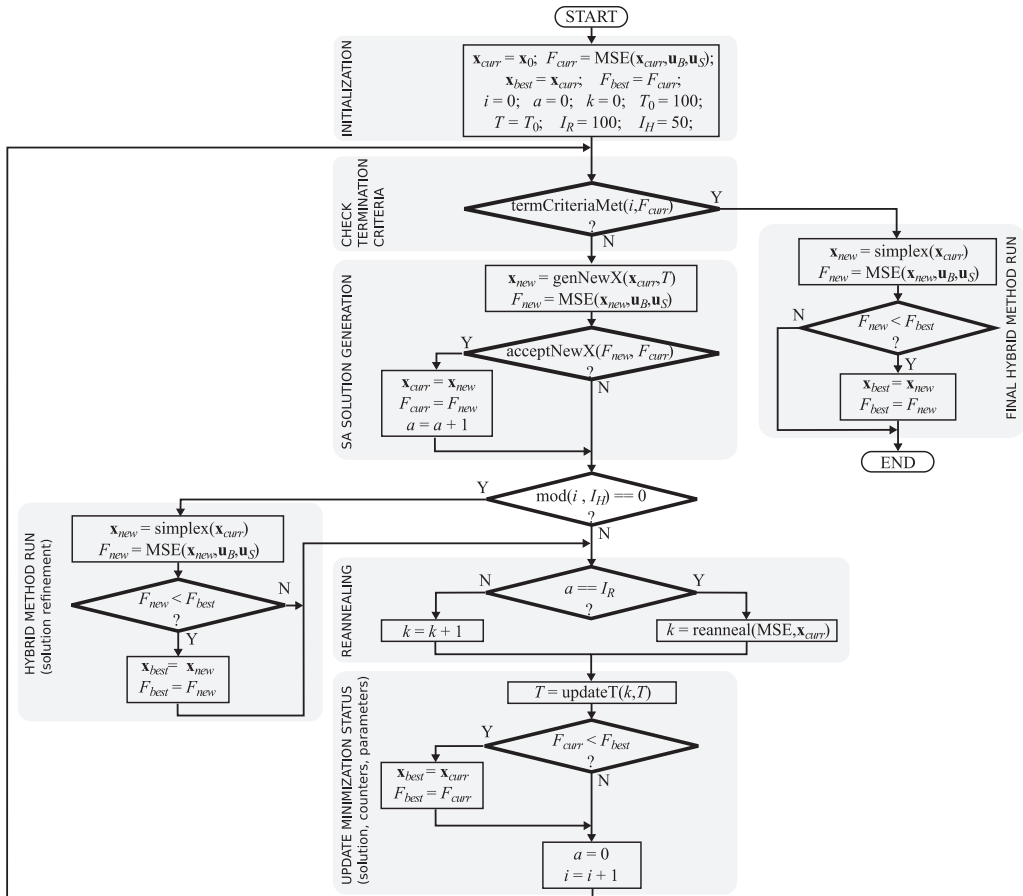


Fig. 9. A diagram of the SASC minimization algorithm.

In each iteration of the main loop the function $\text{genNewX}()$ generates a new SA solution \mathbf{x}_{new} by randomizing \mathbf{x}_{curr} with a scale T . The function $\text{acceptNewX}()$ always accepts better solutions and conditionally accepts also worse ones. The probability of acceptance depends on a current T . Every I_H iterations a hybrid method in the form of $\text{simplex}()$ function is executed. The simplex

search starts at \mathbf{x}_{curr} and returns \mathbf{x}_{new} . When MSE in \mathbf{x}_{new} is better than in \mathbf{x}_{best} then \mathbf{x}_{best} and F_{best} are updated to \mathbf{x}_{new} and F_{new} , respectively.

By most of time T decreases with each iteration according to the rule $T(i+1) = T(i) \cdot 0.95^k$. The exception is for the reanneal() function, which can indirectly (by decreasing k) cause an increase of T . This prevents the algorithm from getting stuck in a local minimum. Reannealing is executed every I_R accepted solutions.

4. Performance verification

The performance of the model (3) identified with the proposed SASC technique is proven by the comparison of voltage waveform reconstruction errors with errors obtained with ANN models presented in [8]. Both physical model and compared ANNs were identified/trained on the same datasets to enable the direct comparison of these two approaches. The main difference between compared models (physical model and ANNs) is such that the physical model has a structure reflecting the real object structure and its parameters have a physical interpretation, while ANN is a black-box model, whose structure and parameters have no physical meaning. Maximum errors (MAXE) and root-mean-squared errors (RMSE):

$$RMSE_p = \sqrt{\frac{1}{N} \sum_{n=1}^N (\hat{\mathbf{u}}_B(p, n) - \mathbf{u}_B(p, n))^2}, \quad (5)$$

$$MAXE_p = \max_n |\hat{\mathbf{u}}_B(p, n) - \mathbf{u}_B(p, n)|, \quad (6)$$

were adopted as performance measures of the busbar voltage reconstruction quality. They were calculated separately for each phase. Additionally an aggregated performance index in the form of MSE (4), was calculated for each test case.

The following models capable of busbar voltage reconstruction were selected for the comparison:

1. Non-opt. – model (3) using parameters obtained with the direct measurement;
2. SASC-SS – model (3) identified with the SASC technique on the SS dataset;
3. SASC-SD – model (3) identified with the SASC technique on the SD dataset;
4. LYRC-5-L – the best layer-recurrent ANN trained on the SD dataset from [8].

Each of compared methods was verified using noiseless (SS, SD) and noisy (SSN, SDN) verification datasets. The values of errors (5), (6) and a performance index of busbar voltage reconstruction obtained for each of compared methods are shown in Table 2.

4.1. MSE comparison results

From Table 2 it can be seen that the performance of physical models SASC-SS and SASC-SD is significantly better than that of LYRC-5-L network and the non-optimized model.

In noiseless conditions, the aggregated performance index (MSE) value of the SASC-SD physical model is more than 8 times better than the best-performance LYRC-5-L network for the SD verification dataset and 33 times better for the SS verification dataset. In noisy conditions the superiority of SASC-SD over LYRC-5-L is even higher (20 and 40 times, respectively).

Table 2. Comparison of busbar voltage waveform reconstruction methods (DT stands for dataset).

Method	Ident DT	Noiseless input signals							Noisy input signals								
		Ver. DT	RMSE [%]			MAXE [%]			Perf. Ind. MSE	Ver. DT	RMSE [%]			MAXE [%]			Perf. Ind. MSE
			X	Y	Z	X	Y	Z			X	Y	Z	X	Y	Z	
Non-opt.	-	SS	5.29	3.51	4.90	13.7	46.7	38.0	0.862	SSN	5.35	3.58	4.96	13.9	46.9	38.1	0.865
		SD	3.86	2.52	3.52	42.7	36.8	16.7	0.438	SDN	3.92	2.57	3.58	43.0	36.9	16.5	0.439
SASC-SS	SS	SS	0.21	0.15	0.19	0.64	0.53	0.57	0.001	SSN	0.30	0.26	0.29	1.41	1.20	1.38	0.003
		SD	0.48	0.24	0.29	16.3	15.1	12.9	0.005	SDN	0.50	0.28	0.33	16.3	15.0	12.9	0.006
SASC-SD	SD	SS	0.17	0.17	0.19	0.40	0.40	0.42	0.001	SSN	0.28	0.30	0.31	1.29	1.51	1.38	0.003
		SD	0.24	0.24	0.24	14.0	13.8	28.0	0.002	SDN	0.28	0.29	0.30	14.1	13.9	27.8	0.003
LYRC-5-L	SD	SS	0.91	0.77	1.29	3.87	2.88	5.13	0.043	SSN	1.98	1.24	2.18	10.2	6.24	10.7	0.138
		SD	0.73	0.61	0.76	37.0	40.4	45.3	0.020	SDN	1.45	0.89	1.51	43.0	43.5	47.9	0.070
LYRC-5-S	SS	SS	0.25	0.17	0.20	1.24	0.69	0.95	0.005	SSN	3.44	1.52	2.25	16.6	8.15	11.2	0.26
		SD	2.32	1.95	1.18	75.2	39.2	43.7	0.14	SDN	3.60	2.89	2.23	81.0	40.3	44.0	0.35

4.2. Dynamic reconstruction errors

The reconstruction errors of the best SASC-SD model and the best LYRC-5-L ANN from [8] were compared also in dynamic states. Figure 10 shows a superiority of the SASC-SD model over LYRC-5-L ANN. The reconstruction errors obtained in dynamic states with the SASC-SD model are far smaller than those obtained with LYRC-5-L ANN. Moreover, during steady states, the errors of SASC-SD model are close to zero, what is not the case with LYRC-5-L. This feature is desired in energy metering applications, where the integration of even low values over long time can lead to significant errors.

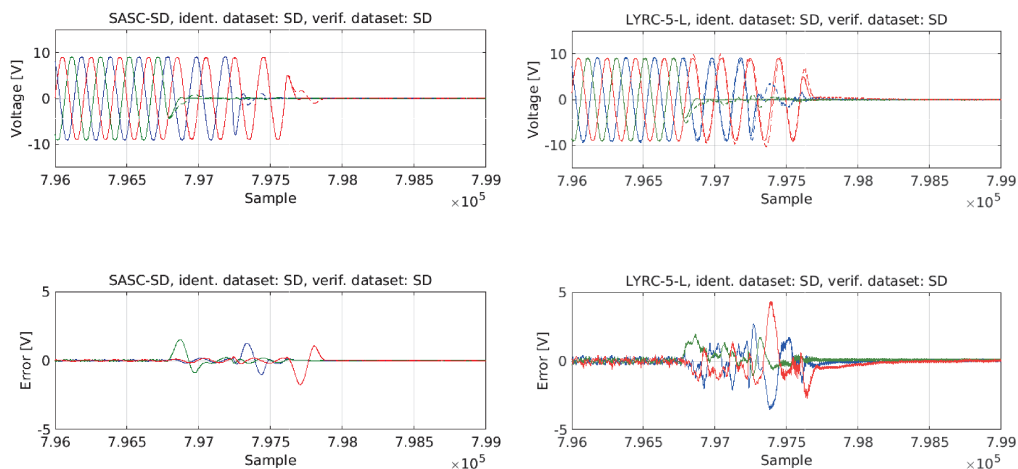


Fig. 10. Comparison of reconstruction errors obtained with SASC-SD model (left) and LYRC-5-L network (right), both identified/trained using SD dataset and tested with SD dataset. The upper plots present actual (continuous) and reconstructed (dashed) busbar voltages, the lower plots present reconstruction errors.

4.3. Frequency domain errors

The reconstruction errors of LYRC-5-L ANN and SASC-SD model were also analysed in the frequency domain. Only the SS dataset was used for the verification in order to limit the share of inter-harmonic components resulting from transients, which are present in the SD datasets. Both reconstructed $\hat{\mathbf{u}}_B(p, n)$ and known $\mathbf{u}_B(p, n)$ bus voltages were divided into 20 ms long (200 samples) segments and transformed using DFT to raw spectra $\hat{\mathbf{U}}_B(p, h)$ and $\mathbf{U}_B(p, h)$, respectively (h denotes the harmonic order). The magnitude and phase angle errors were calculated for both compared methods for each raw spectrum as follows:

$$E_M(p, h) = \frac{||\hat{\mathbf{U}}_B(p, h)| - |\mathbf{U}_B(p, h)||}{|\mathbf{U}_B(p, 1)|}, \quad (7)$$

$$E_A(p, h) = \angle(\hat{\mathbf{U}}_B(p, h)) - \angle(\mathbf{U}_B(p, h)), \quad (8)$$

where $\angle(z)$ denotes an argument of a complex number z .

The results of frequency domain analysis of LYRC-5-L ANN and SASC-SD model are shown in Fig. 11. In the case of amplitude reconstruction errors, also bounds (minimum and maximum errors) from all spectra are shown.

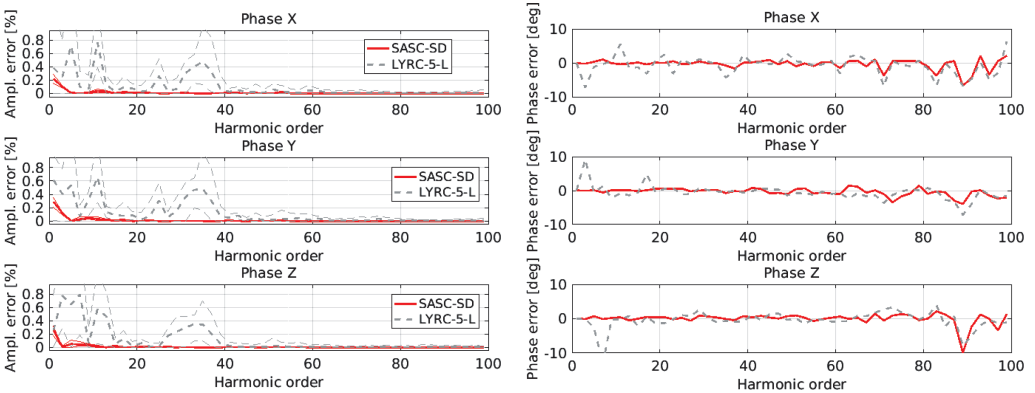


Fig. 11. Errors of magnitude (left) and angle (right) reconstruction in the frequency domain. Thin lines denote error limits, i.e. minimum and maximum errors (SASC-SD solid red, LYRC-5-L dashed grey).

From Fig. 11 it can be seen that SASC-SD exhibits a better performance than LYRC-5-L ANN in terms of both maximum and mean reconstruction errors in the frequency domain (respectively 20 and 12 times lower errors than those of LYRC-5-L). The variance of amplitude reconstruction errors for any frequency is significantly higher for LYRC-5-L ANN than for SASC-SD model. Phase reconstruction errors are also lower for SASC-SD model than for LYRC-5-L ANN (Fig. 11).

4.4. Discussion on identified parameter values versus measured ones

The deviations of optimized parameters obtained with the model identification and those obtained with the direct measurement are summarized in Table 3.

Table 3. Model parameter values obtained with identification compared with the directly measured values.

Parameter	Ident. value	Meas. value	Unit	Ident./meas.	Parameter	Ident. value	Meas. value	Unit	Ident./meas.
C_{X1}	16.2	3.0	fF	5.40	C_{Y5}	55.6	59.7	fF	0.93
C_{X2}	15.6	8.4	fF	1.86	C_{Z1}	61.5	62.0	fF	0.99
C_{X3}	30.4	21.3	fF	1.43	C_{Z2}	36.8	43.5	fF	0.85
C_{X4}	37.5	35.0	fF	1.07	C_{Z3}	30.0	31.2	fF	0.96
C_{X5}	57.0	54.0	fF	1.06	C_{Z4}	27.7	22.6	fF	1.23
C_{Y1}	59.6	57.4	fF	1.04	C_{Z5}	9.6	12.2	fF	0.79
C_{Y2}	50.2	61.0	fF	0.82	B	904.1	900.0	nS	1.00
C_{Y3}	69.6	66.7	fF	1.04	C	725.0	603.0	pF	1.20
C_{Y4}	59.5	65.9	fF	0.90	C_A	287.9	630.0	fF	0.46

Some optimized parameters differ slightly from the measured ones (by a few percent), but some differ much. If we assume that optimized parameters are correct then we can conclude that the measurements were not so precise as it could be inferred from the specifications of the LRC meter.

The differences are a result of inability to perform measurement ideally separated from external sources of errors. The application of a precise LRC meter is not sufficient in the case of an object with a complex geometry or an object with distributed parameters, like an indoor substation. In such experiments there exist stray capacitances, which affect final measurement results. They cannot be easily eliminated, because it would require preparation of very complex shields, drilling additional holes for measurement leads, etc. It is worth mentioning that during measurements of busbar-to-sensor capacitances the differences between results obtained with fully opened overhead compartment doors and those obtained with doors ajar (to enable putting measurement leads inside the compartment) reached 55%. It is noticeable that the greatest differences between values in x_0 and respective values in the identification result are observed for the lowest capacitances in the system, which are most difficult to measure.

Due to nonlinearity of the physical model (3) a simple description of its sensitivity to the parameter values by partial derivatives of the goal function (4) at the optimum is not sufficient. Therefore, its sensitivity was evaluated by observing how does a single parameter change influences the MSE. The parameters were disturbed one-at-a-time by a small deviation, i.e. $\pm 1\%$, $\pm 0.5\%$, $\pm 0.1\%$ or ± 0.05 .

The influence of addeviation of model parameters' values from the optimum on the MSE is shown in Fig. 12. The model is extremely sensitive to variations of some parameters and almost insensitive to variations of others. This explains why an identified parameter value can substantially differ from the measured one. When the model is insensitive to a change of a given parameter, then the goal function is almost flat in the direction related to this parameter, so it is hard to determine the exact minimum of the goal function in this direction.

This is a case of e.g. the capacitance C_A value, which after optimization is less than half of the measured value. Its change from the optimized value almost does not affect the MSE value.

The parameter, that influences MSE most is the capacitance C_{Y3} , which is located in the geometric centre of the system of sensors and busbars. Its deviation by only 1% from the optimum increases MSE about 10 times. It can be concluded that sensor-to-busbar capacitances, for which the air gap between a busbar and a sensor is shortest, affect the model most.

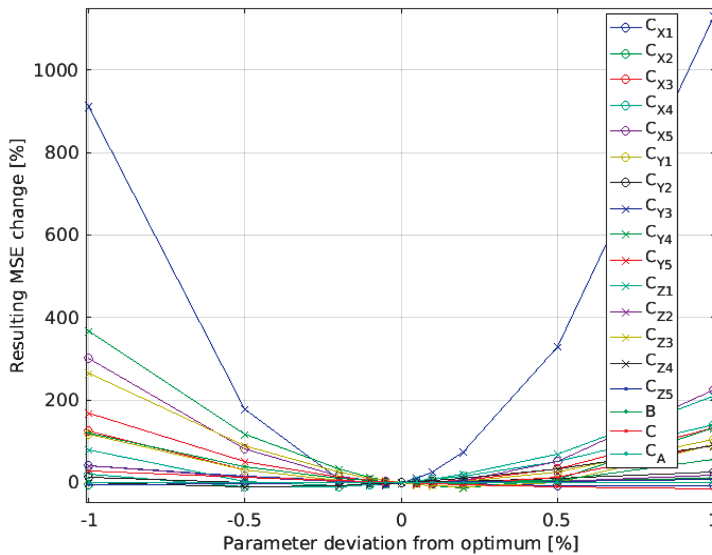


Fig. 12. The model sensitivity shown as an MSE change resulting from deviation of a single parameter value from the optimum.

5. Conclusion

In the paper an improved method for the reconstruction of busbar voltages of an indoor MV substation is presented and validated. The inverse model of conversion performed by EF sensors located in the overhead compartment of the substation is used for the reconstruction. The key to obtain a high reconstruction accuracy is precise identification of the model by a combination of the simulated annealing global optimization and simplex methods. Such a combination, called SASC is proposed after examining several nonlinear optimization techniques. The performance of the reconstruction method is verified by the analysis of busbar voltage reconstruction errors both in time and frequency domains. The best reconstruction accuracy is obtained for the SASC-SD model identified with the SD dataset, containing both steady-state voltages and transients (wideband excitation).

Unlike the methods presented in [3] and [4], aimed at RMS or THD measurement, the method can reconstruct voltage waveforms up to 5 kHz. It outperforms the best-performance LYRC-5-L ANN from [8] by at least 8.7 times in terms of MSE, despite the adverse arrangement of EF sensors. It gives RMS reconstruction errors lower than 0.2% of the fundamental harmonic in noiseless steady-state conditions. It is also a much better result than the one obtained in [3], however the method from [3] bases on auto-calibration, while identification of SASC-SD model requires the use of RVDs for model identification. It is also better than the method [6], which average RMS voltage measurement error is between 0.24% and 2.6%, depending on load type and wire.

Apart from a good voltage reconstruction quality the identification of the physical model with the proposed SASC technique is a dozen times faster than the training of LYRC-5-L ANN. The identified model is stable, what cannot be guaranteed in the case of LYRC ANNs due to feedback. The model is approximately 3 times faster than LYRC-5-L ANN on the same hardware, thus a cheaper CPU can be used for the real-time busbar voltage reconstruction.

The proposed voltage reconstruction method introduces almost no delay (half a sample), thus it is well suited for using in protective automation. It can be used – among others – for the measurement of harmonic impedance of the grid [20], for the tracking of varying grid impedance [21] or in power quality conditioners [22]. The SASC minimization technique itself can be used also in other areas, like e.g. optimal control system design as an alternative to e.g. genetic algorithms [23].

The application of the method is limited to indoor substations, which offer good screening from external electric fields and work in almost stable environmental conditions. Extending the method to outdoor substations would require the design of more complex models taking into account such factors as temperature, humidity, external fields, etc.

References

- [1] Borkowski, D. (2015). A new method for noninvasive measurement of grid harmonic impedance with data selection. *Int. Trans. Electr. Energ. Systems*. 25(12), 3772–3791.
- [2] Locci, N., Muscas, C., Sulis, S. (2009). Experimental comparison of MV voltage transducers for power quality applications. *IEEE Instrumentation and Measurement Technology Conference, 2009. I2MTC '09*. 92–97.
- [3] Bobowski, J.S., Ferdous, M.S., Johnson T. (2015) Calibrated singlecontact voltage sensor for high-voltage monitoring applications. *IEEE Trans. Instrum. and Meas.*, 64(4).
- [4] Tsang, K., Chan, W. (2011). Dual capacitive sensors for non-contact{AC}voltage measurement. *Sensors and Actuators A: Physical*, 167(2), *Solid-State Sensors, Actuators and Microsystems Workshop*, 261–266.
- [5] Chen, K.L., Xu, W. (2016). Voltage distortion measurement using a contactless sensor. *2016 IEEE Power and Energy Society General Meeting (PESGM)*.
- [6] Brunelli, D., Villani, C., Balsamo, D., Benini, L. (2016). Non-invasive voltage measurement in a three-phase autonomous meter. *Microsystem Technologies*, 1–12.
- [7] Wu, L., Wouters, P., van Heesch, E., Steennis, E. (J 2011). On-site voltage measurement with capacitive sensors on high voltage systems. *PowerTech 2011 IEEE Trondheim*, 1–6.
- [8] Borkowski, D., Wetula, A., Bien, A. (2015). Contactless measurement of substation busbars voltages and waveforms reconstruction using electric field sensors and artificial neural network. *IEEE Trans. Smart Grid*. 6(3), 1560–1569.
- [9] Morawski, R. (1991). Unified approach to measurement signal reconstruction. *Measurement*. 9(3), 140–144.
- [10] Jakubiec, J., Makowski, P., Roj, J. (2009). Error model application in neural reconstruction of nonlinear sensor input signal. *IEEE Trans. Instrum. Meas.*, 58(3), 649–656.
- [11] Faifer, M., Ottoboni, R., Prioli, M., Toscani, S. (2016). Simplified modelling and identification of nonlinear systems under quasi-sinusoidal conditions. *IEEE Trans. Instrum. Meas.*, 65(6).
- [12] Adeniran, A.A., Ferik, S.E. (2016) Modeling and identification of nonlinear systems: A review of the multimodel approach – part 1. *IEEE Trans. Systems, Man, and Cybernetics: Systems*, PP(99).
- [13] Nelles, O. (2001). *Nonlinear System Identification: From Classical Approaches to Neural Networks and Fuzzy Models*. Berlin: Springer-Verlag.
- [14] Li, D.H., Fukushima, M. (1999). On the global convergence of BFGS method for nonconvex unconstrained optimization problems. *SIAM Journal on Optimization*, 11(4), 1154–1164.
- [15] Wright, H.M., (September 2004). The interior-point revolution in optimization: History, recent developments, and lasting consequences. *Bulletin of the American Mathematical Society*, 42(1), 39–56.

- [16] Lagarias, J.C., Reeds, J.A., Wright, M.H., Wright, P.E. (1998). Convergence properties of the nelder-mead simplex method in low dimensions. *SIAM Journal of Optimization*, 9(1), 112–147.
- [17] Kirkpatrick, S., Gelatt, C.D., Vecchi, M.P. (1983). Optimization by simulated annealing. *SCIENCE*, 220(4598), 671–680.
- [18] Ingber, L. (1993). Simulated annealing: Practice versus theory. *Mathematical and Computer Modelling*. 18(11) 29–57.
- [19] Neto, A.S., Junior, J.L., Soeiro, F.J.C.P., Neto, L.B., Santana, C.C., Lobato, F.S., Valder, Junior, S. (2010). Application of simulated annealing and hybrid methods in the solution of inverse heat and mass transfer problems. *Simulated Annealing, Theory with Applications*.
- [20] Borkowski, D., Wetula, A., Kowalski, J. (2015). Uncertainty estimation in noninvasive measurement of harmonic impedance – laboratory studies. *2015 International School on Nonsinusoidal Currents and Compensation (ISNCC)*.
- [21] Borkowski, D., Barcentewicz, S. (2014). Power grid impedance tracking with uncertainty estimation using two stage weighted least squares. *Metrol. Meas. Syst.*, 21(1), 99–110.
- [22] Hartman, M., Hashad, M., Mindykowski, J., Hanzelka, Z., Klempka, R. (2005). A new concept of the electrical distributed system for power quality improvement. *CPE'05 Conference Proceedings*, Gdańsk.
- [23] Borkowski, D., Wetula, A., Bien, A. (2012). Design, optimization, and deployment of a waterworks pumping station control system, *ISA Transactions*. 51(4), 539–549.